Clouds and the Earth's Radiant Energy System (CERES)

Algorithm Theoretical Basis Document

An Algorithm for Longwave Surface Radiation Budget for Total Skies
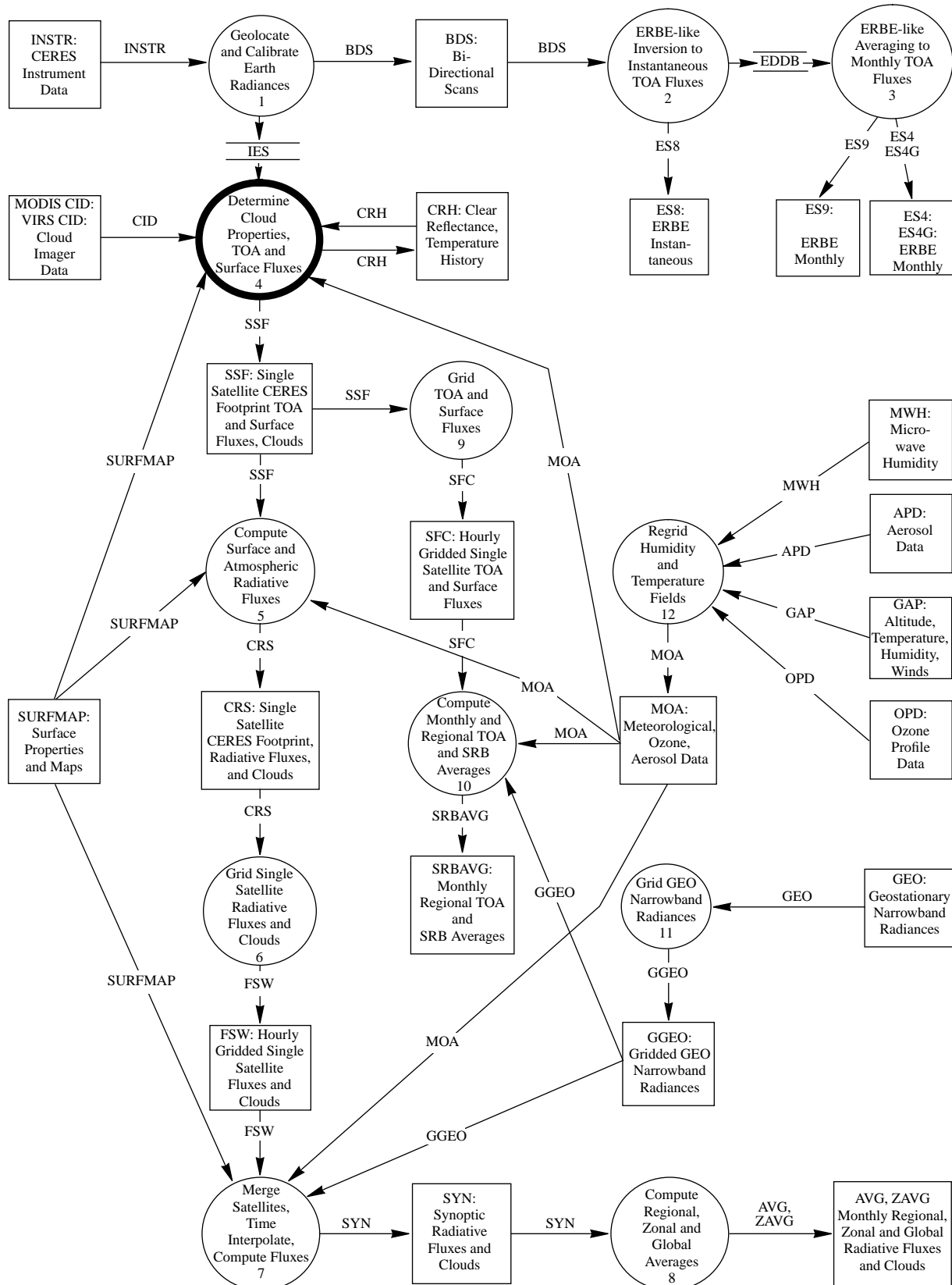
(Subsystem 4.6.3)

Shashi K. Gupta[1]
Charles H. Whitlock[2]
Nancy A. Ritchey[1]
Anne C. Wilber[1]

[1]Analytical Services & Materials, Inc., One Enterprise Parkway, Suite 300, Hampton, Virginia 23666
[2]Atmospheric Sciences Division, NASA Langley Research Center, Hampton, Virginia 23681-0001

June 2, 1997

CERES Top Level Data Flow Diagram

TOA
SW Net
Flux

MOA
Precipitable
Water

Estimate
SW Net Flux
at Surface
4.6.1

Surface SW Fluxes
(Net and Downwelling)

Clear-Sky
TOA LW Flux,
Window Radiance

MOA
Surface Temperature,
Atmos Temperature Profile,
Precipitable Water,
Tropospheric Precipitable Water

Estimated
Clear-Sky
LW Surface
Fluxes
4.6.2

CERES Footprint
Record

Cloudy
Surface LW Fluxes
(Net and Downwelling)

Cloudy
TOA LW Flux,
Window Radiance

MOA
Surface Temperature,
Atmos Temperature Profile,
Humidity Profile

Estimate
Cloudy-Sky
LW Surface
Fluxes
4.6.3

Fractional Cloud Cover,
Cloud Base Pressure,
Cloud Top Pressure,
Cloud Top Temperature
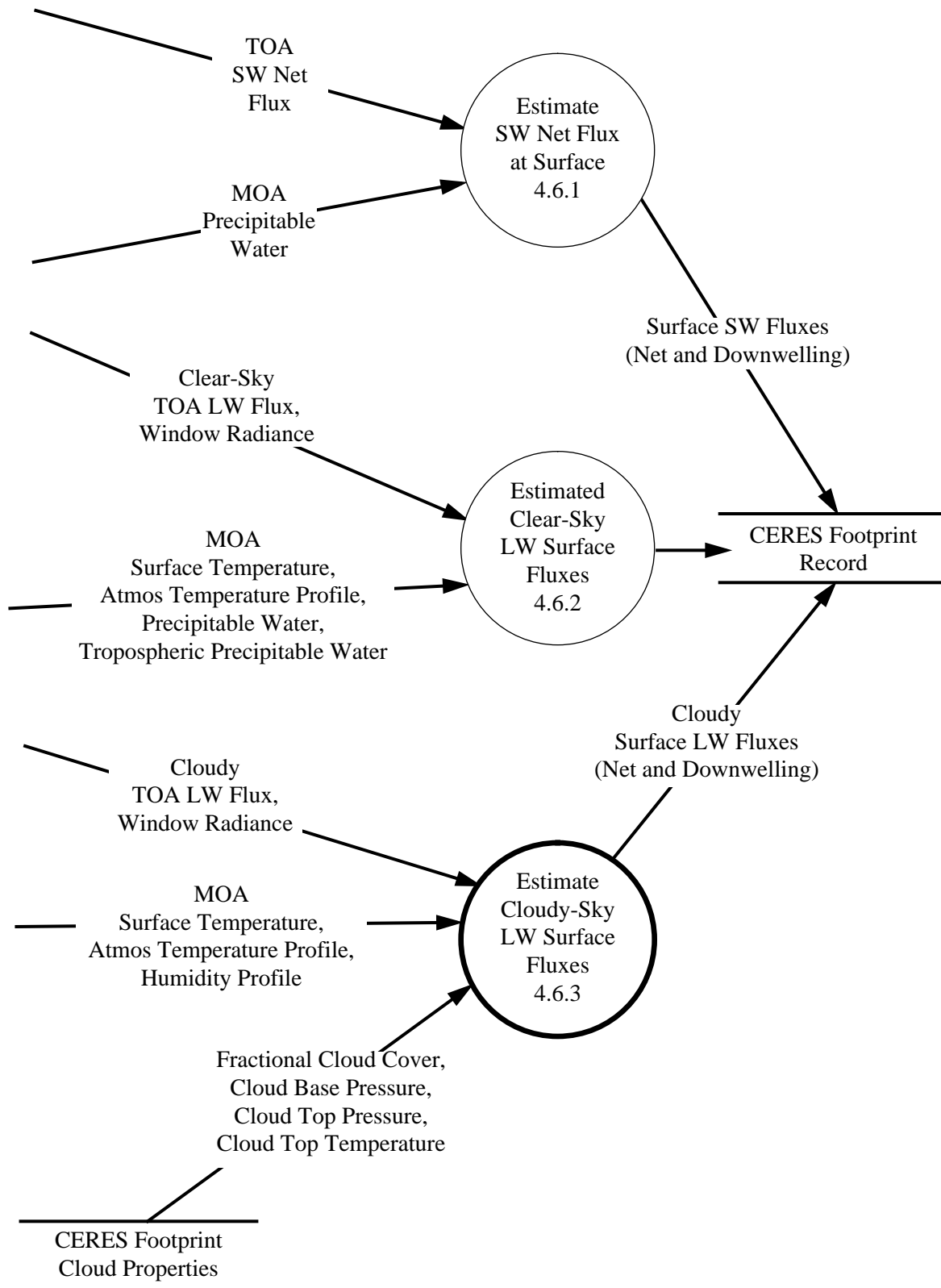
CERES Footprint
Cloud Properties

Figure 4.6-1. Major processes for empirical estimation of SW and LW surface radiation budget.

Abstract

The algorithm described here was developed for deriving global fields of downward and net longwave (LW) radiative fluxes at the Earth's surface. It will be used to compute LW Surface Radiation Budget (SRB), along with other algorithms which use the Clouds and the Earth's Radiant Energy System (CERES) LW window channel (subsystem 4.6.2) and full-column Global Change Model-type (GCM) radiative transfer computations (subsystem 5.0).

The main inputs for this algorithm are surface temperature and emissivity, atmospheric profiles of temperature and humidity, fractional cloud amounts, and cloud heights. The algorithm is flexible so as to be adaptable to the use of input data from a wide variety of sources.

The main outputs of this algorithm are the downward and net LW fluxes at the surface. In this subsystem, these fluxes are produced for each CERES footprint and labeled respectively as Model B downward and net surface LW fluxes in the Single Satellite CERES Footprint TOA and Surface Fluxes (SSF) archival product. Downstream, these fluxes are easily converted to the desired spatial and temporal averages.

This algorithm is based on parameterized equations developed expressly for computing surface LW fluxes in terms of meteorological parameters conveniently available from satellite and/or other operational sources. Also, these equations are soundly based in the physics of radiative transfer, as they were developed from a large database of surface fluxes computed with an accurate narrowband radiative transfer model. This algorithm is currently being used with meteorological inputs from the International Satellite Cloud Climatology Projects-C1 (ISCCP) and -D1 datasets. For CERES processing, all meteorological inputs except cloud parameters and surface emissivity will be available from the Meteorology Ozone and Aerosol (MOA) archival product. Cloud parameters for CERES on Tropical Rainfall Measuring Mission (TRMM) will come from Visible Infrared Scanner (VIRS) and, for CERES on Earth Observing System (EOS-AM/EOS-PM) from Moderate-Resolution Imaging Spectroradiometer (MODIS-N). Surface emissivity for EOS-AM and EOS-PM processing may also come from MODIS-N products. For TRMM processing, however, surface emissivity data are being generated by combining available laboratory measurements with surface-type maps.

4.6.3. An Algorithm for Longwave Surface Radiation Budget for Total Skies

4.6.3.1. Introduction

Net longwave radiative flux at the Earth's surface is a significant component of the surface energy budget. It affects in varying measures, the surface temperature fields, the surface fluxes of latent and sensible heat, the atmospheric and oceanic general circulation, and the hydrological cycle (Suttles and Ohring 1986). In recognition of its importance, the World Climate Research Program (WCRP) has established the Surface Radiation Budget Climatology Project with the goal of developing long-term global databases of surface LW as well as SW radiative fluxes. Such scientific significance makes surface LW fluxes a highly desirable product for the CERES Project.

4.6.3.2. Background

In the framework of CERES processing, the most desirable method would be to derive surface radiative fluxes from the Top-of-Atmosphere (TOA) flux measurements, made directly by CERES instruments. Use of such schemes would confer on surface products, the distinction of being based on direct observation. Such schemes have been used with considerable success for deriving surface shortwave (SW) flux, based on correlations between net SW fluxes at the TOA and the surface (Cess et al. 1991; Li et al. 1993). The validity of such correlations is in serious question at present because of the unresolved issues regarding the magnitude of the SW absorption in clouds (Li and Moreau 1996; see also subsystem 4.6.1). Irrespective of the state of SW correlations, no correlations have been established between TOA and surface LW fluxes. Even though there has been considerable effort in this direction (Ramanathan 1986), there are no accepted algorithms for retrieving surface LW fluxes from TOA LW fluxes alone, even for clear-sky conditions. Such schemes are even less likely to work in the presence of clouds, because strong absorption of LW radiation in the clouds results in a complete decoupling of the LW radiation fields at the TOA and the surface (Stephens and Webster 1984).

An alternative approach for deriving surface LW fluxes is to compute them using radiative transfer models with meteorological data. Keeping in view the accuracy requirements and the volume of processing to be done for CERES, the radiative transfer model has to be computationally fast while maintaining high accuracy. The meteorological inputs have to be available on a global scale, preferably from operational sources. The algorithm described here meets the above requirements fully. It is based on a fast, parameterized computation scheme developed from an accurate narrowband radiative transfer model (Gupta 1989), and is compatible with most sources of operational meteorological data. Recently, this algorithm was selected by the GEWEX/SRB Workshop for producing, on an experimental basis, long-term datasets of surface LW fluxes for use by the climate science community (WCRP 1994).

4.6.3.3. Input Sources and Outputs

The basic inputs to this algorithm are surface temperature and emissivity, temperature and humidity profiles, fractional cloud amounts, and cloud-top heights. Cloud-base heights and water vapor burden below the cloud base are derived from the above parameters as described in the next section. The algorithm was structured originally to utilize TIROS Operational Vertical Sounder (TOVS) products, which until the mid-eighties were about the only operational source of global meteorological data (Gupta 1989). Starting in the late-eighties, global ISCCP-C1 datasets (hereafter referred to as C1 data) which represent a synthesis of temperature and humidity profiles from TOVS and ISCCP's retrieval of cloud parameters became available (Rossow and Schiffer 1991). Revised/improved C1 data, also known as ISCCP-D1 datasets (hereafter D1 data) are becoming available in the mid-nineties, and will supersede C1 data. Since this algorithm works with basic meteorological parameters, it was quickly and easily adapted, first to the use of C1 data (Gupta et al. 1992), and recently to the use of D1 data.

For CERES data processing, all meteorological data except cloud parameters and surface emissivity will be available from the MOA archival product. Cloud parameters for CERES processing from TRMM will be retrieved from VIRS, and for EOS-AM and EOS-PM processing from MODIS-N. For processing of EOS-AM and EOS-PM data, surface emissivity data may come from MODIS-N products but for processing of TRMM data, surface emissivity data are being developed by combining laboratory measurements of Salisbury and D'Aria (1992) with surface-type maps (e.g., Olson et al. 1983; Matthews 1983).

Outputs from this algorithm are the downward and net LW fluxes at the surface. In this subsystem, these fluxes will be computed on a CERES footprint basis. In the following subsystems, these fluxes will be averaged over the required spatial grids and time intervals. A version of this algorithm is currently being used by the authors for deriving global fields of surface LW fluxes using D1 data. An example of monthly average fluxes for October 1986 obtained with ISCCP-D1 data is shown on Plate 1.
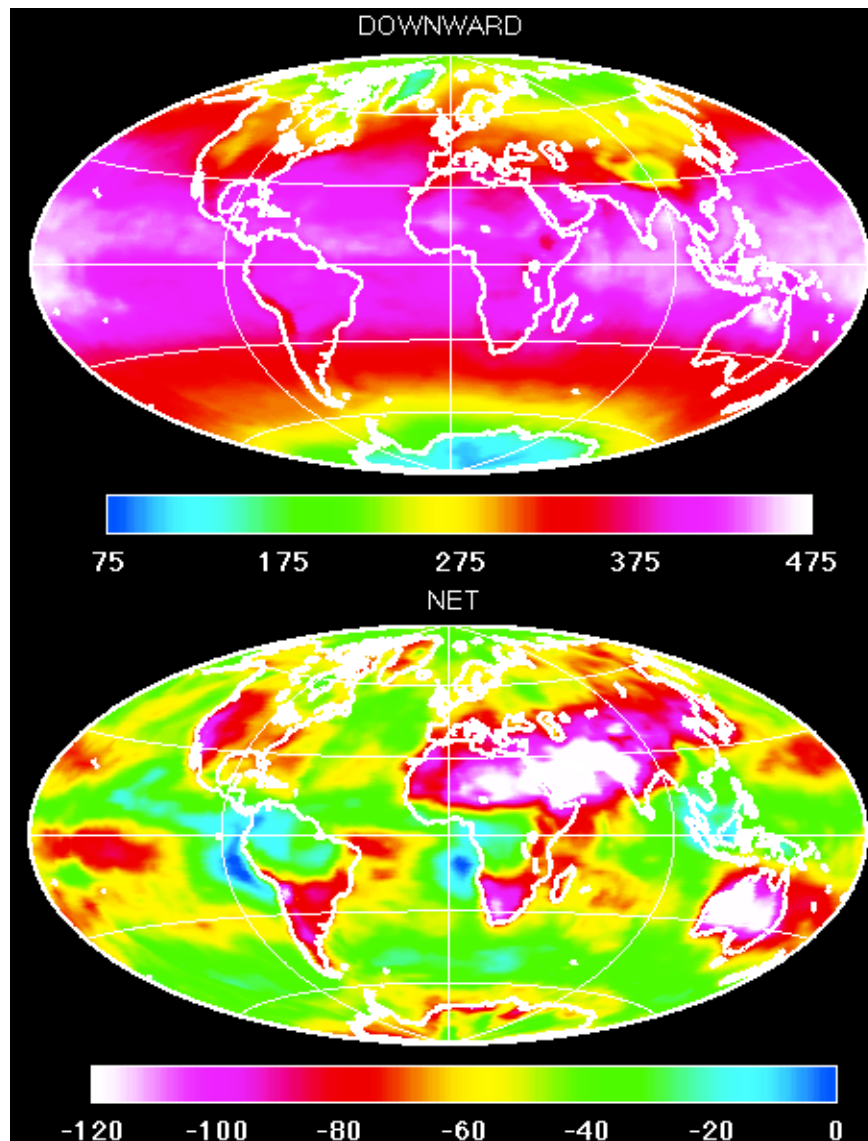
Plate 1. Surface longwave fluxes (W-m^{-2}) monthly averages for October 1986.

4.6.3.4. Algorithm Description

The Downward Longwave Flux (DLF) at the surface, denoted as F_d, is computed as

$$F_d = C_1 + \Sigma C_{21} A_{c1}, \tag{1}$$

where C_1 is the clear-sky DLF, and C_{21} and A_{c1} are the cloud forcing factor and fractional cloud amount respectively for each cloud layer. The summation extends over all layers in which clouds are present. At the spatial resolution of the CERES footprint, the highest frequency is likely to occur for two-layer clouds (see subsystem 4.0). The Net Longwave Flux (NLF), denoted as F_n, is computed as

$$F_n = F_d - \varepsilon_s \sigma T_s^4 - (1 - \varepsilon_s) F_d, \tag{2}$$

where σ is the Stefan-Boltzman constant, ε_s and T_s are the emissivity and temperature of the surface. Parameterizations described below were developed for C_1 and C_{21} in terms of TOVS meteorological parameters which are a part of C1 data.

Clear-sky DLF (C_1) is represented as

$$C_1 = (A_0 + A_1 V + A_2 V^2 + A_3 V^3) \times T_e^{3.7} \qquad (3)$$

where $V = \ln W$, W is the water vapor burden of the atmosphere, T_e is an effective emitting temperature of the atmosphere, and $A_0, A_1, A_2,$ and A_3 are regression coefficients. T_e is computed as

$$T_e = k_s T_s + k_1 T_1 + k_2 T_2, \qquad (4)$$

where T_1 and T_2 are the mean temperatures of the first and second atmospheric layers next to the surface, which correspond to the surface - 800 mb, and 800 - 680 mb regions. The values of the weighting factors k_s, k_1, and k_2 were determined from sensitivity analysis and found to be 0.60, 0.35, and 0.05 respectively. The values of the regression coefficients in equation (3) are

$$A_0 = 1.791 \times 10^{-7},$$

$$A_1 = 2.093 \times 10^{-8},$$

$$A_2 = -2.748 \times 10^{-9},$$

and

$$A_3 = 1.184 \times 10^{-9}.$$

The cloud forcing factor for a layer (C_{21}) is represented as

$$C_{21} = T_{cb}^4 / (B_0 + B_1 W_c + B_2 W_c^2 + B_3 W_c^3) \qquad (5)$$

where T_{cb} is the cloud-base temperature, and W_c is the water vapor burden below the cloud base for the layer under consideration. The values of the regression coefficients are

$$B_0 = 4.990 \times 10^7,$$

$$B_1 = 2.688 \times 10^6,$$

$$B_2 = -6.147 \times 10^3,$$

and

$$B_3 = 8.163 \times 10^2.$$

T_{cb} and W_c are computed from available meteorological profiles using the following procedure. A cloud-base pressure (P_{cb}) is obtained by combining the available cloud-top pressure with climatological estimates of cloud thickness. T_{cb} is obtained by matching P_{cb} against the available temperature profile. W_c is computed from the available humidity profile. For details of the above procedure and the development of equations (3) and (5), the reader is referred to Gupta (1989). All temperature values are in K, and water vapor burden values in kg-m^{-2}.

It was found during the processing of global datasets that the use of equation (5) resulted in significant overestimation of C_{21} for low-level clouds. As long as $(P_s - P_{cb}) > 200$ mb (where P_s is the surface pressure), equation (5) provided accurate results and was used as such. For $(P_s - P_{cb}) \leq 200$ mb, significant overestimation of C_{21} occurred, and was remedied with the following procedure. The maximum possible value of C_{21} (denoted as $C_{2\max}$) occurs for the condition when the cloud base is located at the surface (i.e., $P_s - P_{cb} = 0$). This limiting value is used to constrain the values of the regression coefficients of equation (5). In practice, constraining the value of B_0 was found to be quite adequate. The modified value of B_0 (denoted as B_0') subject to the above constraint is represented as

$$B_0' = T_s^4 / (\sigma T_s^4 - C_1) \qquad (6)$$

The value of B_0' is much larger than B_0, and for $(P_s - P_{cb}) = 0$, it forces the value of C_{21} obtained from equation (5) to match the value of $C_{2\max}$. B_0 continues to yield satisfactory results when $(P_s - P_{cb}) > 200$ mb. For values of $(P_s - P_{cb})$ between 0 and 200 mb, the applicable value of this regression coefficient is obtained by linear interpolation (in pressure) between B_0' and B_0. For a detailed discussion of the steps described above, the reader is referred to Gupta et al. (1992).

4.6.3.5. Accuracy/Error Analysis

Fluxes computed with the above algorithm are subject to random and systematic errors coming from the radiation models as well as the meteorological data. In the context of this algorithm, errors coming from the radiation models can be divided further into those coming from (i) the use of the parameterized equations (3) and (5), and (ii) the detailed radiation model from which those equations were derived.

A reasonable estimate of the errors coming from equations (3) and (5) relative to the detailed model can be obtained by comparing the fluxes computed with the two methods using the same meteorological data. Figure 1 shows such a comparison of DLF values for a set of 330 soundings representing pole-to-pole meteorological conditions, sampled from the global C1 dataset for July 1983. Figure 1 shows that the parameterized model DLF is 1.3 Wm^{-2} higher. The rms difference between the two sets (which includes the bias) is 5.0 Wm^{-2}.

The errors in the fluxes computed from the detailed model come from the spectral line parameters, and the various approximations made in the spectral, angular, and height integration of the radiative transfer equation. Reasonable estimates of the detailed model errors can be obtained in the framework of the Intercomparison of Radiation Codes in Climate Models (ICRCCM) (Ellingson et al. 1991). Figure 2 shows a comparison of DLF values obtained with the detailed model and other ICRCCM results for the 5 climatological profiles. The ordinate represents the ratio of the DLF values for a model to the line-by-line DLF values which are used as reference. Thus, the dashed line represents the reference line-by-line results, the "+" symbols the highest values, and the "×" symbols the lowest values from among the large number of results submitted to the ICRCCM. This comparison shows that the fluxes from the present detailed model (depicted as hollow circles) average about 1% higher than the line-by-line results. This difference is equivalent to a systematic error of about 2-3 Wm^{-2}, which is slightly higher than the difference between the detailed and parameterized model results.
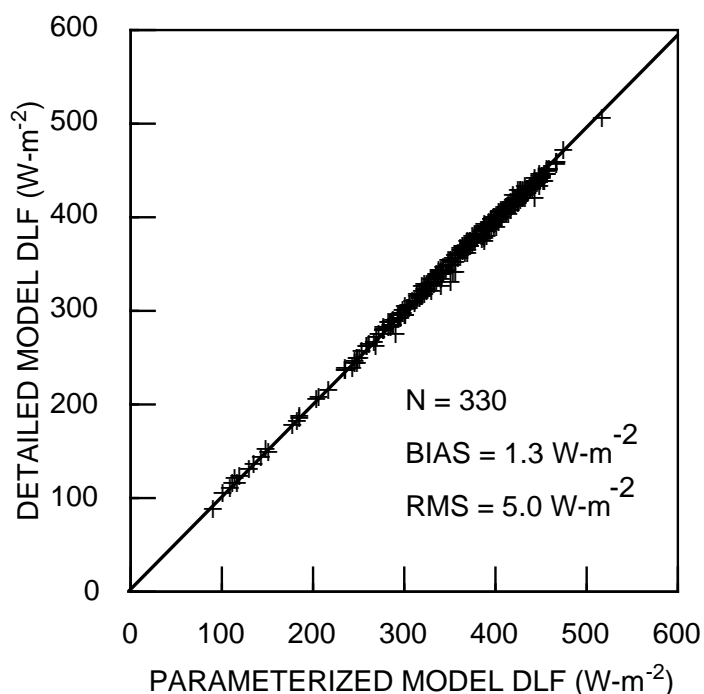
Figure 1. Scatterplot between DLF computed with the parameterized model and the detailed model for 330 soundings sampled from the global C1 data for July 1983.

A brief discussion of the random and systematic errors coming from the meteorological data is presented here. For details, the reader is referred to Gupta et al. (1993). Random errors arising from meteorological data errors on an individual sounding basis were found to be of the order of ± 20 Wm^{-2}. For monthly averages, these reduce to about ± 5 Wm^{-2}. Systematic errors in the fluxes arise from the biases in the meteorological inputs. Biases in the cloud parameters were found to be one of the large sources. Also, if ε_s deviates significantly from unity and realistic values of ε_s are not used, additional bias is incurred in the computation of F_n. The magnitude of this bias is given by

$$\Delta F_n \ = \ (1 - \varepsilon_s)(F_d - \sigma T_s^4) \tag{7}$$

which can be quite large, especially over desert areas.

4.6.3.6. Validation

Historically, finding high quality measurements of surface LW fluxes appropriate for validating radiative transfer algorithms has been very difficult. This situation is beginning to change with the establishment of measurement sites by the ARM Program and the WCRP/BSRN. Surface-measured LW flux data were recently obtained from the SGP ARM/CART site and also from the BSRN, and used for validating the present algorithm.

Figure 3 shows a comparison of the algorithm results with surface measurements acquired at the SGP ARM/CART site in Oklahoma during the April 1994 Intensive Observing Period (IOP). These data are available from the CERES/ARM/GEWEX Experiment (CAGEX; Charlock and Alberta 1996).
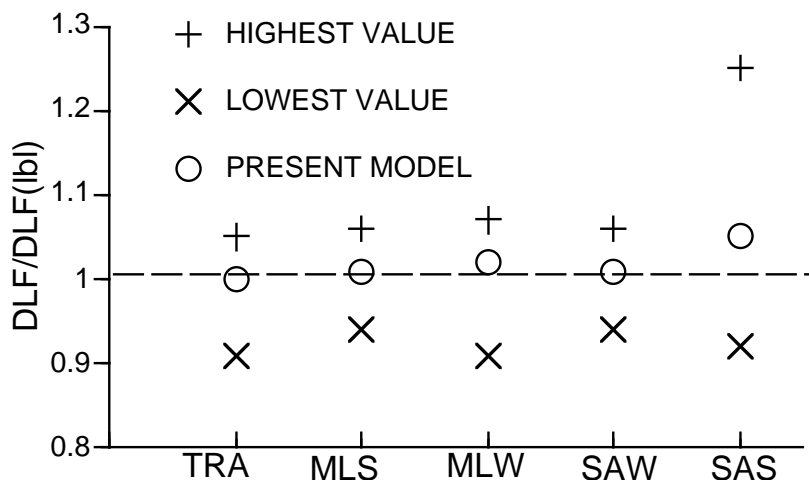
Figure 2. Comparison of clear-sky DLF obtained with the detailed model and line-by-line and other ICRCCM results for the five climatological profiles (TRA - tropical; MLS - mid-latitude summer; MLW - mid-latitude winter; SAW - sub-arctic winter; SAS - sub-arctic summer).

Corresponding meteorological data (except clouds) were obtained from the National Weather Service network soundings in the area. Coincident cloud parameters were derived from GOES-7 radiances by Minnis et al. (1995). Comparison of 30-minute averages of surface measurements over a period of 26 days and corresponding results from the algorithm shows a bias of -3 Wm^{-2} and a rms difference of 21 Wm^{-2}.

Figure 4 shows a comparison of the algorithm results with monthly average surface-measured fluxes for three months in 1992 (January, July, and October) from seven sites located in diverse climate regimes around the globe. Surface measurements were obtained from the Baseline Surface Radiation Network (BSRN). Coincident meteorological parameters used in the algorithm were taken from the D1 data. Comparison of 15 site-month pairs shows a bias of 6 Wm^{-2} and a rms difference of 21 Wm^{-2}.

With the establishment of new Atmospheric Radiation Measurement (ARM) sites in the Tropical West Pacific (TWP) and the North Slope of Alaska (NSA), and the expansion of the BSRN, large amounts of high quality surface-measured data should soon become available. It is planned to use these data for validating the algorithm results during pre-launch and post-launch periods.

4.6.3.7. Strategic Concerns and Remedies

The apparent weaknesses of the algorithm, e.g., the overestimation of C_{21} for low-level clouds have been remedied as described earlier. The weighting scheme of equation (4) is designed to minimize the errors in the presence of strong temperature discontinuities at the surface. Realistic values of surface emissivity are being obtained by combining laboratory measurements available in the literature with global surface-type maps. Remaining uncertainties in surface temperature and emissivity over land areas are still important concerns, but have to await further advances in retrieval algorithms for their res-olutions. Satellite and/or operational meteorological datasets sometimes have large gaps, and fill values (e.g., -999.) are frequently substituted in the data streams where real data are missing. Unchecked, this would generally result in absurd values for output parameters. These conditions will be largely reme-died in the preparation of the MOA database (see subsystem 12.0) where appropriate interpolation pro-cedures will be used to fill most data gaps. Any remaining problems will be handled in this subsystem
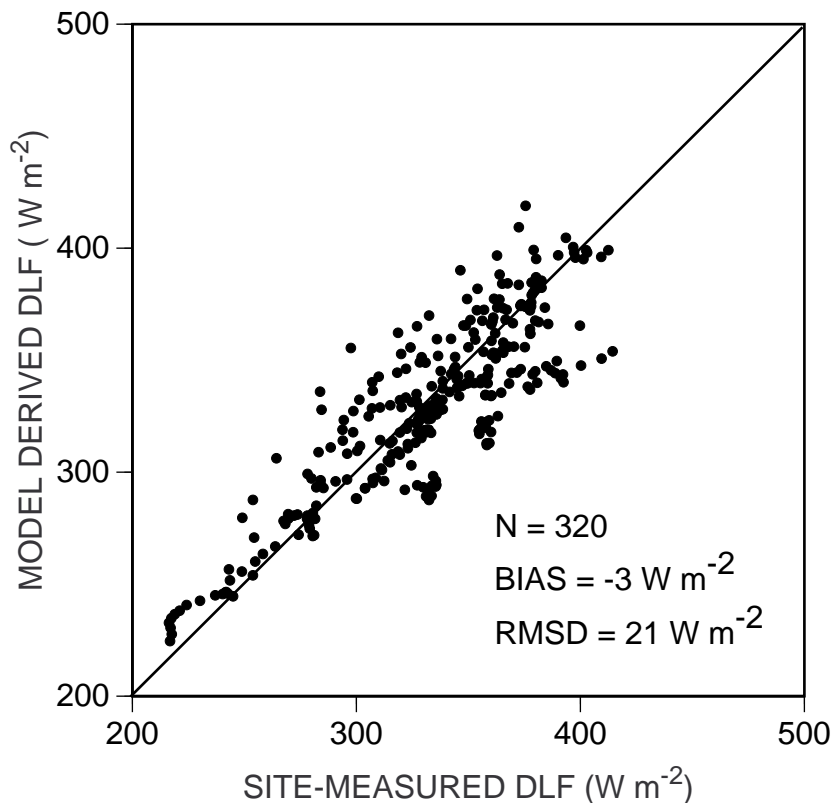
Figure 3. Comparison between site-measured DLF from the SGP ARM/CART site during the April 1994 IOP and correspond-
ing results from the present algorithm.

by checking all important input parameters against carefully chosen high and low limits. The limits are
chosen to encompass the normal spatial and temporal variabilities of these parameters. When an input
parameter falls outside the above limits, another attempt is made to generate a replacement (in place of
the fill value) by interpolation between nearest neighbors or from climatology. When these attempts
fail, the input and output data are rejected and excluded from the averages.

4.6.3.8. Concluding Remarks

The algorithm described here is currently operational with D1 data as inputs and has been used in the
past with C1 data. Error analysis of the output products shows that errors coming from the meteorologi-
cal inputs are considerably larger than those coming from the parameterized equations. With improved
meteorological inputs available from MOA, and cloud parameters from VIRS and MODIS-N, we
expect the errors in CERES estimates of surface LW fluxes to be considerably lower than those achiev-
able presently. Use of realistic values of surface emissivity (instead of unity used in the earlier work) is
expected to further reduce the errors. Also, an ongoing effort aimed at validating this algorithm against
surface measurements from the ARM program and the BSRN during the pre-launch and post-launch
periods is planned. Surface LW fluxes obtained with this algorithm would constitute a valuable CERES
product by themselves, and would also be useful for independently checking on the quality of the fluxes
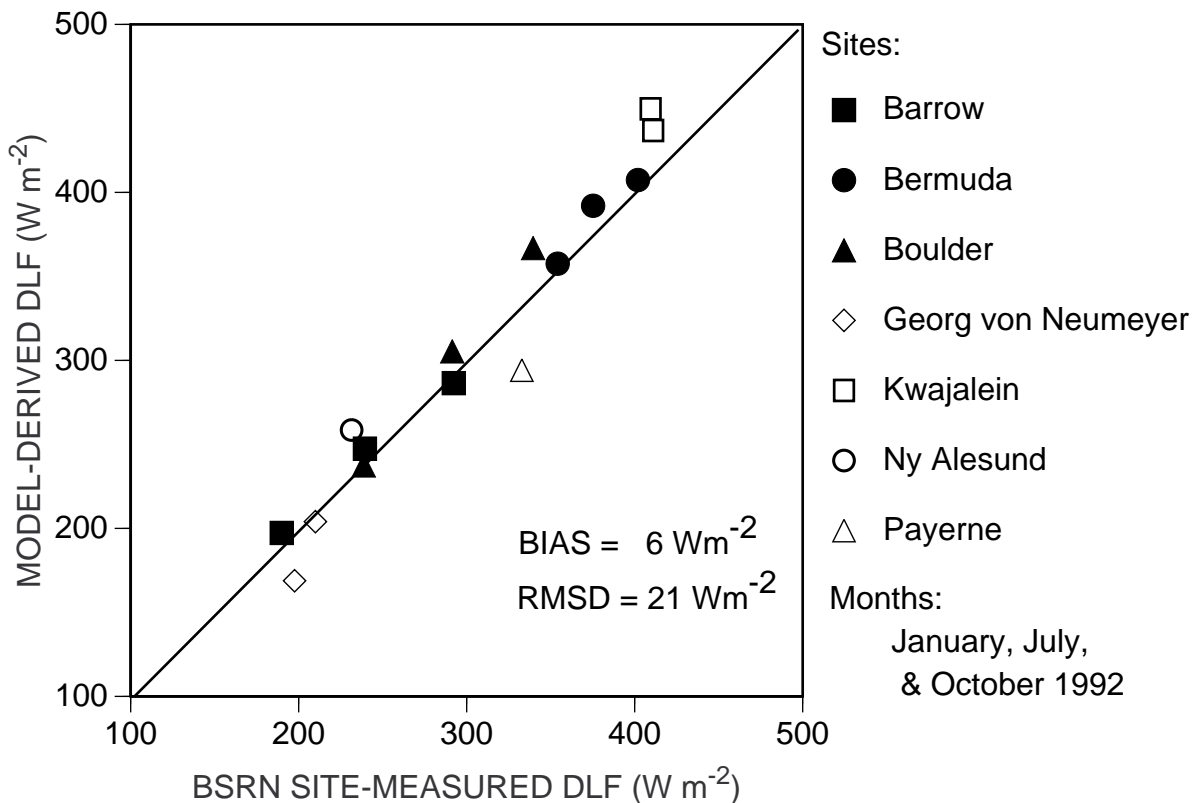obtained from the GCM-type radiative transfer computations.

Figure 4. Comparison between monthly average DLF from seven BSRN sites and corresponding results from the algorithm derived with D1 data.

4.6.3.9. References

Cess, R. D; Dutton, E. G.; DeLuisi, J. J.; and Jiang, F. 1991: Determining Surface Solar Absorption From Broadband Satellite Measurements for Clear Skies—Comparison With Surface Measurements. *J. Climat.*, vol. 4, no. 2, pp. 236–247.

Charlock, T. P.; and Alberta, T. L. 1996: The CERES/ARM/GEWEX Experiment (CAGEX) for the Retrieval of Radiative Fluxes with Satellite Data. *Bull. Amer. Meteor. Soc.*, vol. 77 (accepted for publication).

Ellingson, R. G.; Ellis, J. S.; and Fels, S. B. 1991: The Intercomparison of Radiation Codes Used in Climate Models—Long Wave Results. *J. Geophys. Res.*, vol. 96, no. D5, pp. 8929–8953.

Gupta, S. K. 1989: A Parameterization for Longwave Surface Radiation From Sun-Synchronous Satellite Data. *J. Climat.*, vol. 2, no. 4, pp. 305–320.

Gupta, S. K.; Darnell, W. L.; and Wilber, A. C. 1992: A Parameterization for Longwave Surface Radiation From Satellite Data—Recent Improvements. *J. Appl. Meteorol.*, vol. 31, no. 12, pp. 1361–1367.

Gupta, S. K.; Wilber, A. C.; Darnell, W. L.; and Suttles, J. T. 1993: Longwave Surface Radiation Over the Globe From Satellite Data—An Error Analysis. *Int. J. Remote Sens.*, vol. 14, no. 1, pp. 95–114.

Li, Zhanqing; Leighton, H. G.; Masuda, K.; and Takashima, T. 1993: Estimation of SW Flux Absorbed at the Surface From TOA Reflected Flux. *J. Climat.*, vol. 6, no. 2, pp. 317–330.

Li, Z.; and Moreau, L. 1996: Alteration of Atmospheric Solar Absorption by Clouds: Simulation and Observation. *J. Appl. Meteorol.*, vol. 35, pp. 653-670.

Matthews, E. 1983: Global Vegetation and Land Use: New High Resolution Data Bases for Climate Studies. *J. Clim. Appl. Meteorol.*, vol. 22, pp. 474-487.

Minnis, P.; Smith, W. L., Jr.; Garber, D. P.; Ayers, J. K.; and Doelling, D. R. 1995: Cloud Properties Derived From GOES-7 for Spring 1994 ARM Intensive Observing Period Using Version 1.0.0 of ARM Satellite Data Analysis Program. NASA RP-1366, Washington, DC, 58 pp.

Olson, J. S.; Watts, J.; and Allison, L. 1983: Carbon in Live Vegetation of Major World Ecosystems. W-7405-ENG-26, U. S. Department of Energy, Oak Ridge National Laboratory.

Ramanathan, V. 1986: Scientific Use of Surface Radiation Budget for Climate Studies. *Surface Radiation Budget for Climate Applications*, J. T. Suttles and G. Ohring, eds., NASA RP-1169, pp. 58–86.

Rossow, W. B.; and Schiffer, R. A. 1991: ISCCP Cloud Data Products. *Bull. Am. Meteorol. Soc.*, vol. 72, no. 1, pp. 2–20.

Salisbury, J. W.; and D'Aria, D. M. 1992: Emissivity of Terrestrial Materials in the 8 - 14 Micron Atmospheric Window. *Remote Sens. Environ.*, vol. 42, pp. 83-106.

Stephens, G. L.; and Webster, P. J. 1984: Cloud Decoupling of the Surface and Planetary Radiative Budgets. *J. Atmos. Sci.*, vol. 41, no. 4, pp. 681–686.

Suttles, J. T.; and Ohring, G. 1986: *Surface Radiation Budget for Climate Applications.* NASA RP-1169, Washington, DC, 136 pp.

WCRP; 1994: Report of the Fifteenth Session of the Joint Scientific Committee, Geneva, Switzerland, 14-18 March 1994, WMO/TD-No. 632, pp. 35-36.

Appendix A

Nomenclature

Acronyms

ADEOS	Advanced Earth Observing System
ADM	Angular Distribution Model
AIRS	Atmospheric Infrared Sounder (EOS-AM)
AMSU	Advanced Microwave Sounding Unit (EOS-PM)
APD	Aerosol Profile Data
APID	Application Identifier
ARESE	ARM Enhanced Shortwave Experiment
ARM	Atmospheric Radiation Measurement
ASOS	Automated Surface Observing Sites
ASTER	Advanced Spaceborne Thermal Emission and Reflection Radiometer
ASTEX	Atlantic Stratocumulus Transition Experiment
ASTR	Atmospheric Structures
ATBD	Algorithm Theoretical Basis Document
AVG	Monthly Regional, Average Radiative Fluxes and Clouds (CERES Archival Data Product)
AVHRR	Advanced Very High Resolution Radiometer
BDS	Bidirectional Scan (CERES Archival Data Product)
BRIE	Best Regional Integral Estimate
BSRN	Baseline Surface Radiation Network
BTD	Brightness Temperature Difference(s)
CCD	Charge Coupled Device
CCSDS	Consultative Committee for Space Data Systems
CEPEX	Central Equatorial Pacific Experiment
CERES	Clouds and the Earth's Radiant Energy System
CID	Cloud Imager Data
CLAVR	Clouds from AVHRR
CLS	Constrained Least Squares
COPRS	Cloud Optical Property Retrieval System
CPR	Cloud Profiling Radar
CRH	Clear Reflectance, Temperature History (CERES Archival Data Product)
CRS	Single Satellite CERES Footprint, Radiative Fluxes and Clouds (CERES Archival Data Product)
DAAC	Distributed Active Archive Center
DAC	Digital-Analog Converter

DAO	Data Assimilation Office
DB	Database
DFD	Data Flow Diagram
DLF	Downward Longwave Flux
DMSP	Defense Meteorological Satellite Program
EADM	ERBE-Like Albedo Directional Model (CERES Input Data Product)
ECA	Earth Central Angle
ECLIPS	Experimental Cloud Lidar Pilot Study
ECMWF	European Centre for Medium-Range Weather Forecasts
EDDB	ERBE-Like Daily Data Base (CERES Archival Data Product)
EID9	ERBE-Like Internal Data Product 9 (CERES Internal Data Product)
EOS	Earth Observing System
EOSDIS	Earth Observing System Data Information System
EOS-AM	EOS Morning Crossing Mission
EOS-PM	EOS Afternoon Crossing Mission
ENSO	El Niño/Southern Oscillation
ENVISAT	Environmental Satellite
EPHANC	Ephemeris and Ancillary (CERES Input Data Product)
ERB	Earth Radiation Budget
ERBE	Earth Radiation Budget Experiment
ERBS	Earth Radiation Budget Satellite
ESA	European Space Agency
ES4	ERBE-Like S4 Data Product (CERES Archival Data Product)
ES4G	ERBE-Like S4G Data Product (CERES Archival Data Product)
ES8	ERBE-Like S8 Data Product (CERES Archival Data Product)
ES9	ERBE-Like S9 Data Product (CERES Archival Data Product)
FLOP	Floating Point Operation
FIRE	First ISCCP Regional Experiment
FIRE II IFO	First ISCCP Regional Experiment II Intensive Field Observations
FOV	Field of View
FSW	Hourly Gridded Single Satellite Fluxes and Clouds (CERES Archival Data Product)
FTM	Functional Test Model
GAC	Global Area Coverage (AVHRR data mode)
GAP	Gridded Atmospheric Product (CERES Input Data Product)
GCIP	GEWEX Continental-Phase International Project
GCM	General Circulation Model
GEBA	Global Energy Balance Archive
GEO	ISSCP Radiances (CERES Input Data Product)

GEWEX	Global Energy and Water Cycle Experiment
GLAS	Geoscience Laser Altimetry System
GMS	Geostationary Meteorological Satellite
GOES	Geostationary Operational Environmental Satellite
HBTM	Hybrid Bispectral Threshold Method
HIRS	High-Resolution Infrared Radiation Sounder
HIS	High-Resolution Interferometer Sounder
ICM	Internal Calibration Module
ICRCCM	Intercomparison of Radiation Codes in Climate Models
ID	Identification
IEEE	Institute of Electrical and Electronics Engineers
IES	Instrument Earth Scans (CERES Internal Data Product)
IFO	Intensive Field Observation
INSAT	Indian Satellite
IOP	Intensive Observing Period
IR	Infrared
IRIS	Infrared Interferometer Spectrometer
ISCCP	International Satellite Cloud Climatology Project
ISS	Integrated Sounding System
IWP	Ice Water Path
LAC	Local Area Coverage (AVHRR data mode)
LaRC	Langley Research Center
LBC	Laser Beam Ceilometer
LBTM	Layer Bispectral Threshold Method
Lidar	Light Detection and Ranging
LITE	Lidar In-Space Technology Experiment
Lowtran 7	Low-Resolution Transmittance (Radiative Transfer Code)
LW	Longwave
LWP	Liquid Water Path
MAM	Mirror Attenuator Mosaic
MC	Mostly Cloudy
MCR	Microwave Cloud Radiometer
METEOSAT	Meteorological Operational Satellite (European)
METSAT	Meteorological Satellite
MFLOP	Million FLOP
MIMR	Multifrequency Imaging Microwave Radiometer
MISR	Multiangle Imaging Spectroradiometer
MLE	Maximum Likelihood Estimate
MOA	Meteorology Ozone and Aerosol

MODIS	Moderate-Resolution Imaging Spectroradiometer
MSMR	Multispectral, multiresolution
MTSA	Monthly Time and Space Averaging
MWH	Microwave Humidity
MWP	Microwave Water Path
NASA	National Aeronautics and Space Administration
NCAR	National Center for Atmospheric Research
NCEP	National Centers for Environmental Prediction
NESDIS	National Environmental Satellite, Data, and Information Service
NIR	Near Infrared
NMC	National Meteorological Center
NOAA	National Oceanic and Atmospheric Administration
NWP	Numerical Weather Prediction
OLR	Outgoing Longwave Radiation
OPD	Ozone Profile Data (CERES Input Data Product)
OV	Overcast
PC	Partly Cloudy
POLDER	Polarization of Directionality of Earth's Reflectances
PRT	Platinum Resistance Thermometer
PSF	Point Spread Function
PW	Precipitable Water
RAPS	Rotating Azimuth Plane Scan
RPM	Radiance Pairs Method
RTM	Radiometer Test Model
SAB	Sorting by Angular Bins
SAGE	Stratospheric Aerosol and Gas Experiment
SARB	Surface and Atmospheric Radiation Budget Working Group
SDCD	Solar Distance Correction and Declination
SFC	Hourly Gridded Single Satellite TOA and Surface Fluxes (CERES Archival Data Product)
SHEBA	Surface Heat Budget in the Arctic
SPECTRE	Spectral Radiance Experiment
SRB	Surface Radiation Budget
SRBAVG	Surface Radiation Budget Average (CERES Archival Data Product)
SSF	Single Satellite CERES Footprint TOA and Surface Fluxes, Clouds
SSMI	Special Sensor Microwave Imager
SST	Sea Surface Temperature
SURFMAP	Surface Properties and Maps (CERES Input Product)
SW	Shortwave

SWICS	Shortwave Internal Calibration Source
SYN	Synoptic Radiative Fluxes and Clouds (CERES Archival Data Product)
SZA	Solar Zenith Angle
THIR	Temperature/Humidity Infrared Radiometer (Nimbus)
TIROS	Television Infrared Observation Satellite
TISA	Time Interpolation and Spatial Averaging Working Group
TMI	TRMM Microwave Imager
TOA	Top of the Atmosphere
TOGA	Tropical Ocean Global Atmosphere
TOMS	Total Ozone Mapping Spectrometer
TOVS	TIROS Operational Vertical Sounder
TRMM	Tropical Rainfall Measuring Mission
TSA	Time-Space Averaging
UAV	Unmanned Aerospace Vehicle
UT	Universal Time
UTC	Universal Time Code
VAS	VISSR Atmospheric Sounder (GOES)
VIRS	Visible Infrared Scanner
VISSR	Visible and Infrared Spin Scan Radiometer
WCRP	World Climate Research Program
WG	Working Group
Win	Window
WN	Window
WMO	World Meteorological Organization
ZAVG	Monthly Zonal and Global Average Radiative Fluxes and Clouds (CERES Archival Data Product)

Symbols

A	atmospheric absorptance
$B_\lambda(T)$	Planck function
C	cloud fractional area coverage
CF_2Cl_2	dichlorofluorocarbon
$CFCl_3$	trichlorofluorocarbon
CH_4	methane
CO_2	carbon dioxide
D	total number of days in the month
D_e	cloud particle equivalent diameter (for ice clouds)
E_o	solar constant or solar irradiance
F	flux

f	fraction
G_a	atmospheric greenhouse effect
g	cloud asymmetry parameter
H_2O	water vapor
I	radiance
i	scene type
m_i	imaginary refractive index
$\hat{N}$	angular momentum vector
N_2O	nitrous oxide
O_3	ozone
P	point spread function
p	pressure
Q_a	absorption efficiency
Q_e	extinction efficiency
Q_s	scattering efficiency
R	anisotropic reflectance factor
r_E	radius of the Earth
r_e	effective cloud droplet radius (for water clouds)
r_h	column-averaged relative humidity
S_o	summed solar incident SW flux
S_o'	integrated solar incident SW flux
T	temperature
T_B	blackbody temperature
t	time or transmittance
W_{liq}	liquid water path
w	precipitable water
$\hat{x}_o$	satellite position at t_o
x, y, z	satellite position vector components
$\dot{x}, \dot{y}, \dot{z}$	satellite velocity vector components
z	altitude
z_{top}	altitude at top of atmosphere
α	albedo or cone angle
β	cross-scan angle
γ	Earth central angle
γ_{at}	along-track angle
γ_{ct}	cross-track angle
δ	along-scan angle
ε	emittance
Θ	colatitude of satellite

θ	viewing zenith angle
θ_o	solar zenith angle
λ	wavelength
μ	viewing zenith angle cosine
μ_o	solar zenith angle cosine
ν	wave number
ρ	bidirectional reflectance
τ	optical depth
$\tau_{aer}(p)$	spectral optical depth profiles of aerosols
$\tau_{H_2O\lambda}(p)$	spectral optical depth profiles of water vapor
$\tau_{O_3}(p)$	spectral optical depth profiles of ozone
Φ	longitude of satellite
ϕ	azimuth angle
$\tilde{\omega}_o$	single-scattering albedo

Subscripts:

c	cloud
cb	cloud base
ce	cloud effective
cld	cloud
cs	clear sky
ct	cloud top
ice	ice water
lc	lower cloud
liq	liquid water
s	surface
uc	upper cloud
λ	spectral wavelength

Units

AU	astronomical unit
cm	centimeter
cm-sec^{-1}	centimeter per second
count	count
day	day, Julian date
deg	degree
deg-sec^{-1}	degree per second
DU	Dobson unit
erg-sec^{-1}	erg per second
fraction	fraction (range of 0–1)

g	gram
g-cm^{-2}	gram per square centimeter
g-g^{-1}	gram per gram
g-m^{-2}	gram per square meter
h	hour
hPa	hectopascal
K	Kelvin
kg	kilogram
kg-m^{-2}	kilogram per square meter
km	kilometer
km-sec^{-1}	kilometer per second
m	meter
mm	millimeter
μm	micrometer, micron
N/A	not applicable, none, unitless, dimensionless
ohm-cm^{-1}	ohm per centimeter
percent	percent (range of 0–100)
rad	radian
rad-sec^{-1}	radian per second
sec	second
sr^{-1}	per steradian
W	watt
W-m^{-2}	watt per square meter
W-m^{-2}sr^{-1}	watt per square meter per steradian
W-m^{-2}sr^{-1}μm^{-1}	watt per square meter per steradian per micrometer